Journal of Molecular and Cellular Cardiology 77 (2014) 178–191

Contents lists available at ScienceDirect

Journal of Molecular and Cellular Cardiology

journal homepage: www.elsevier.com/locate/yjmcc

Original article

Image-based evaluation of contraction–relaxation kinetics of human-induced pluripotent stem cell-derived cardiomyocytes: Correlation and complementarity with extracellular electrophysiology

Tomohiro Hayakawa [a,*,1], Takeshi Kunihiro [a,1], Tomoko Ando [b], Seiji Kobayashi [a], Eriko Matsui [a], Hiroaki Yada [a], Yasunari Kanda [b], Junko Kurokawa [b], Tetsushi Furukawa [b,**]

[a] Medical Business Unit, Sony Corporation, 1-5-45 Yushima, Bunkyo-ku, Tokyo 113-8510, Japan
[b] Department of Bio-informational Pharmacology, Medical Research Institute, Tokyo Medical and Dental University, 1-5-45 Yushima, Bunkyo-ku, Tokyo 113-8510, Japan

ARTICLE INFO

Article history:
Received 27 July 2014
Accepted 10 September 2014
Available online 23 September 2014

Keywords:
Human-induced pluripotent stem cell-derived cardiomyocytes
Motion vector prediction
Traction force microscopy
Ca^{2+} transient
Field potential
Multi-electrode arrays

ABSTRACT

In this study, we used high-speed video microscopy with motion vector analysis to investigate the contractile characteristics of hiPS-CM monolayer, in addition to further characterizing the motion with extracellular field potential (FP), traction force and the Ca^{2+} transient. Results of our traction force microscopy demonstrated that the force development of hiPS-CMs correlated well with the cellular deformation detected by the video microscopy with motion vector analysis. In the presence of verapamil and isoproterenol, contractile motion of hiPS-CMs showed alteration in accordance with the changes in fluorescence peak of the Ca^{2+} transient, i.e., upstroke, decay, amplitude and full-width at half-maximum. Simultaneously recorded hiPS-CM motion and FP showed that there was a linear correlation between changes in the motion and field potential duration in response to verapamil (30–150 nM), isoproterenol (0.1–10 μM) and E-4031 (10–50 nM). In addition, tetrodotoxin (3–30 μM)-induced delay of sodium current was corresponded with the delay of the contraction onset of hiPS-CMs. These results indicate that the electrophysiological and functional behaviors of hiPS-CMs are quantitatively reflected in the contractile motion detected by this image-based technique. In the presence of 100 nM E-4031, the occurrence of early after-depolarization-like negative deflection in FP was also detected in the hiPS-CM motion as a characteristic two-step relaxation pattern. These findings offer insights into the interpretation of the motion kinetics of the hiPS-CMs, and are relevant for understanding electrical and mechanical relationship in hiPS-CMs.

1. Introduction

Human-induced pluripotent stem cell-derived cardiomyocytes (hiPS-CMs) and human embryonic stem cell-derived cardiomyocyte (hES-CMs) hold promise for the applications in cardiac cell biology [1], drug development [2–6] and cardiac therapeutics [7–11]. To date, hiPS-/hES-CMs have been characterized largely based on studies that examined the aspects of the electrophysiology or the Ca^{2+} signaling/handling [3,12–20]. This is in contrast to the contractile characteristics of the hiPS-/hES-CMs, as there have been few studies performed at the present time [21–29]. Limited numbers of studies, however, demonstrated that hES-CMs showed chronotropy but no significant inotropy in response to β-adrenoceptor agonist, isoproterenol, by using a force transducer for three-dimensionally (3D) engineered hES-CM tissue [29] or for co-culture system of hES-CMs with non-contractile slices of neonatal murine ventricles [28]. These results suggest the importance of performing a phenotype evaluation for hiPS-/hES-CMs based on the contractile properties as well as electrophysiological characteristics to assess their adaptability to the applications. In addition, a report that used atomic force microscopy to investigate two-dimensionally (2D) cultured hiPS-CMs from patients with dilated cardiomyopathy (DCM) demonstrated that the DCM hiPS-CM exhibited a phenotype that was based on the perturbed contractility rather than on the electrophysiological abnormality [27,30]. This demonstrated the need for developing methodologies that characterize the electrical and mechanical relationship of hiPS-/hES-CMs.

In our current study, we combined phase-contrast video microscopy and multi-electrode array (MEA) measurement in order to investigate the relationship between the contractile motion and the extracellular

Abbreviations: ADD, average deformation distance; CM, cardiomyocyte; CRD, contraction–relaxation duration; FP, field potential; FPD, field potential duration; FP_{slow}, slow signal component of FP; FWHM, full-width at half-maximum; hiPS-CM, human-induced pluripotent stem cell-derived cardiomyocyte; hES-CM, human embryonic stem cell-derived cardiomyocyte; MCS, maximum contraction speed; MEA, multi-electrode array; MRS, maximum relaxation speed; PIV, particle image velocimetry; TF, traction force; TFM, traction force microscopy; TTX, tetrodotoxin.

* Corresponding author. Tel.: +81 3 5803 4791; fax: +81 3 5803 4790.
** Corresponding author. Tel.: +81 3 5803 4950; fax: +81 3 5803 0364.
E-mail addresses: tomohiro.hayakawa@jp.sony.com (T. Hayakawa), t_furukawa.bip@mri.tmd.ac.jp (T. Furukawa).
[1] These authors contributed equally.

http://dx.doi.org/10.1016/j.yjmcc.2014.09.010

electrophysiology of the 2D-cultured hiPS-CMs under various cardioactive agents. The label-free video microscopy is a method of choice for evaluating the contractile characteristics of CMs, and many researchers have reported the applicability in various culture conditions [31–40]. For example, for isolated rod-shaped adult CMs, the shortening length and velocity of contraction of whole cell body or sarcomere were evaluated quantitatively using video microscopy with edge-detection technique [34,41–43]. Edge-detection method was also applied to the contractility estimation of embryonic bodies with hES-CMs [44,45]. Kamgoue et al. applied image correlation analysis for single adult and neonatal rat CMs, and detected intracellular strains quantitatively from the calculated 2D displacement field [36]. Modified image correlation analysis was developed by Ahola et al. for single hiPS-CMs, which exhibits heterogeneous in shape, to evaluate the detailed intracellular deformation [46]. Beating frequency of mouse ES-CM monolayer has been evaluated based on the image analysis of transmitted light intensity change [35] and the fast Fourier transform technique [39]. Meanwhile, we have previously reported the applicability of image correlation analysis, or motion vector analysis, for analyzing video images of neonatal rat CM monolayers [47]. By calculating the velocity field over the whole image, this method has made it possible to evaluate the average contractile speed, global deformation and contraction propagation in the CM monolayer with high spatiotemporal resolution [47]. Due to the convenience and non-invasiveness, such label-free video microscopies would be advantageous for the readout method of hiPS-/hES-CM behaviors, especially for the applications in therapeutics and drug safety assessment. In addition, since microscope observation itself does not interfere with the electrophysiological measurements, video microscopies are amenable to the simultaneous measurement with electrical measurements, e.g., patch clamping and MEA, to gain greater insight into the electro-mechanical correlations of CMs.

In this study, we further performed traction force microscopy and Ca^{2+} imaging in the hiPS-CMs in order to discuss the association of contractile motion to force development and Ca^{2+} transient, respectively. Our results showed that electrophysiological and functional behaviors of the 2D-cultured hiPS-CMs are quantitatively reflected by contractile motions detected with high-speed video microscopy. These findings offer insights into the interpretation of motion kinetics of hiPS-CMs, and are relevant for understanding electrical and mechanical relationship in hiPS-CMs. These results also demonstrate that it is possible for us to broaden the scope of application for hiPS-CMs for use in even simple culture conditions.

2. Materials and methods

2.1. hiPS-CMs and cell preparation

The hiPS-CMs used in this study were purchased from Cellular Dynamics International, Inc. (CDI) (iCell Cardiomyocytes, CDI, Madison, WI, USA). The iCell CMs are highly purified human CMs (>98% pure cardiomyocytes) that are derived from iPS cells using previously described differentiation and purification protocols [48]. The iCell CMs were seeded and maintained according to the protocol recommended by the supplier using iCell Cardiomyocytes Plating Medium (CDI) and iCell Cardiomyocytes Maintenance Medium (CDI) at 37 °C, 7% CO_2. The details on the cell preparation for MEA recordings, Ca^{2+} transient measurements and TFM are provided in the Supplementary materials.

2.2. Video microscopy

A high-speed digital CMOS camera (KP-FM400WCL, Hitachi Kokusai Denki Engineering, Tokyo, Japan) was mounted on an inverted microscope (Eclipse Ti, Nikon, Tokyo, Japan). Movie images of beating hiPS-CMs were recorded as sequential phase-contrast images with a 10× objective at a frame rate of 150 fps, a resolution of 2048 × 2048 pixels, and a depth of 8 bits. Further details on the video imaging are provided in the Supplementary materials.

2.3. Motion vector analysis

Motion vectors of beating hiPS-CMs were obtained using a block matching algorithm, as has been described elsewhere [47,49]. Further details on the motion vector analysis are provided in the Supplementary materials.

2.4. Traction force microscopy

2.4.1. Fabrication of polyacrylamide hydrogel substrates and hiPS-CM seeding

Polyacrylamide hydrogel substrates containing fluorescence beads (#G0100, 1 μm diameter, Ex/Em = 468/508 nm, Duke Scientific Co., CA, USA) were fabricated in accordance with previously reported methods [26,50,51]. Further details on the methods are provided in the Supplementary materials.

2.4.2. Traction force microscopy

Video of the hiPS-CMs cultured on polyacrylamide gel was captured using phase-contrast and fluorescence microscopy to detect contractile motion and substrate deformation, respectively. Estimation of the force development of hiPS-CMs was performed by a particle image velocimetry (PIV) [52] and Fourier transform traction cytometry (FTTC) [51–53] programs implemented as an ImageJ plugin. Details are provided in the Supplementary materials.

2.5. Simultaneous recordings of FP and motion

MED probes (MED-P515A, Alpha MED Sciences, Osaka, Japan) equipped with platinum black-coated 64 planar microelectrodes that were arranged in an 8 × 8 grid embedded in the center of a transparent glass plate were used for extracellular recordings of the FP from the CM monolayer [54]. The details on the cell preparation for MEA recordings are provided in the Supplementary materials. Image acquisitions and multi-electrode array (MEA) recordings were synchronized using external triggering options of the MEA system. Data were recorded simultaneously for the 64 electrodes (sampling frequency; 20 kHz, bandwidth; 1–1000 Hz) and were analyzed by Mobius Software (Alpha MED Sciences) in order to detect the field potential duration (FPD). In this study, we averaged at least 10 consecutive FP waveforms to evaluate the field potential parameters. The details on the simultaneous measurements are also provided in the Supplementary materials.

2.6. Calcium imaging

For imaging of the Ca^{2+} transient in the hiPS-CMs, iCell Cardiomyocytes (CDI) were plated in a 96-well plate pre-coated with rat collagen type I (BD, Franklin lakes, NJ) at a density of 3×10^4 cells/well (cultured with 100 μl medium). hiPS-CMs were loaded with Fluo-5F/AM (Invitrogen, Carlsbad, CA, USA) dissolved in dimethylsulfoxide (DMSO, WAKO Pure Chemical, Osaka, Japan) and added to the culture medium at a concentration of 5 μM in preparation for the Ca^{2+} imaging. After 30 min incubation, the culture dishes were placed on a microscope stage (IX-71, Olympus, Tokyo, Japan). Ca^{2+} fluorescence images were captured with a digital CCD camera (CoolSNAP HQ2, Photometrics, Tucson, AZ, USA) at a resolution of 696 × 520 pixels and 33 fps using a 20× objective and recorded using MetaMorph software (Molecular Devices, Sunnyvale, CA, USA). The data were then quantified as the background subtracted fluorescence intensity changes (ΔF) normalized to the baseline fluorescence (F_0) using the ImageJ software and the KaleidaGraph software ver. 4.1.1 (Synergy Software, Reading, PA, USA). Amplitudes, full-width at half-

maximum, maximal upstroke and the decay of the Ca^{2+} transient were also analyzed with the KaleidaGraph software.

2.7. Cardioactive substances

Isoproterenol was purchased from Sigma (St. Louis, MO, USA), E-4031 and tetrodotoxin from WAKO Pure Chemical Industries, and verapamil from Nacalai Tesque (Kyoto, Japan). Stock solutions for isoproterenol and E-4031 were prepared in distilled water, while verapamil was prepared in DMSO. All stock solutions were further diluted in culture medium, with the final concentration of DMSO less than 0.05%. Four to six increasing concentrations of the test substances were applied consecutively for 10 min each.

2.8. Statistical analysis

Data are compared to control in the paired *t*-test for the grouped data. Data are presented as means ± SEM. The value was expressed as a percentage of the control value, while the comparison was made using raw values of each parameter. We considered *p* values less than 0.05 to be statistically significant.

3. Results

3.1. Motion vector detection as a reliable representation of contractile characteristics of hiPS-CMs

3.1.1. Motion vector detection from the movie image of single hiPS-CMs

We first evaluated the contractile motion of single hiPS-CMs. Sparsely plated hiPS-CMs exhibited heterogeneous shapes and a variety of sizes (Fig. 1A). Fig. 1B shows an example of single hiPS-CM motion detected by the motion vector analysis. As indicated by the motion vectors that overlay the image of hiPS-CM, cellular deformation generally occurred toward the center direction of the cell body during contraction process (Fig. 1B (1)). After a transient pause of cellular motion (Fig. 1B (2)), the cell body returned to the position of resting state, exhibiting a slower motion speed than that observed during contraction (Fig. 1A (3)). By averaging the magnitude of motion vectors and plotting them against time, we were able to obtain information on the contraction and relaxation motion (Fig. 1C), along with the frequency (Fig. 1D). Although the contraction and relaxation occurs in the opposite direction, the average of vector magnitude is a positive value, thereby resulting in a two-positive peak profile that reflects the contraction–relaxation process. As seen in Fig. 1E, we are able to extract various parameters regarding contractile motion from this two-peak motion profile. Our current study primarily examined four parameters of this hiPS-CM motion. These included the maximum values of the average magnitude of motion vectors during the contraction (a) and relaxation (b) processes (termed MCS; maximum contraction speed and MRS; maximum relaxation speed, respectively), the total area under two peaks (c) (representing the average deformation distance (ADD) during the contraction–relaxation process), and the duration of contraction and relaxation motion (d) (with the duration between the onset of the contraction peak and the offset of the relaxation peak defined as the contraction–relaxation duration (CRD)). Fig. 1F–I shows contractile parameters of single hiPS-CMs ($n = 40$) cultured in physiological condition (37 °C and 5% CO_2). Single hiPS-CMs exhibited beating rate ranging from ~20 to ~110 beats per minute (bpm) with the average of 62 bpm. Analysis of motion vectors showed that the average values of MCS, MRS, CRD and ADD were 8.2 μm/s, 4.1 μm/s, 455 ms and 1.07 μm, respectively, and the average cell area was found to be 4244.3 μm^2. We examined to plot the cell area against MCS and MRS, and found that contractile speeds were not significantly dependent on the cell area (Fig. 1K). CRD of single hiPS-CMs showed a linear correlation with the beating rate with the correlation coefficient of 0.768 (Fig. 1L).

3.1.2. Contractile motion and traction force of the hiPS-CMs

Subsequently, we used traction force microscopy (TFM) to assess whether the cellular deformation, detected by phase-contrast microscopy and motion vector analysis, was correlated with the force development of hiPS-CMs on the elastic substrate (polyacrylamide gel). Fig. 2 shows a typical image of a hiPS-CM on the gel substrate (12 kPa) examined by phase-contrast (a) and fluorescence microscopy (b). Typical images of displacement and traction force fields that were calculated from the two fluorescence images (taken before and after contraction) are also shown in Fig. 2A(c) and (d), respectively. We then compared the ADD and the traction force of hiPS-CMs on the elastic substrate (12 kPa and 50 kPa). As shown in Fig. 2B, a linear correlation was observed for the traction force and the ADD of the single hiPS-CMs cultured on gel substrates, with a correlation coefficient of 0.737 ($n = 13$) and 0.595 ($n = 12$) for the hiPS-CMs on the 12 kPa and 50 kPa substrates, respectively. These results suggested that the cellular deformation detected with motion vector analysis could be used as a surrogate of the traction force developed by the hiPS-CM contraction.

3.1.3. Ca^{2+} transient and contractile motion of hiPS-CMs

To verify the relationship between the contractile motion and the cytoplasmic Ca^{2+} concentration, we further examined the parameters of the Ca^{2+} transient of the hiPS-CMs. Fig. 3A and B show the typical examples of Ca^{2+} transient and motion waveform of hiPS-CMs, respectively, in the absence and the presence of 100 nM isoproterenol. Isoproterenol altered the amplitude, maximum upstroke, maximum decay and full-width at half-maximum (FWHM) of the Ca^{2+} transient with 113, 114, 157 and 84% of the control, respectively (see bar charts in Fig. 3A). Isoproterenol also altered the contractile parameters, i.e., ADD, MCS, MRS and CRD were changed to 113, 124, 146 and 80% of the control, respectively (Fig. 3B). In contrast, verapamil (100 nM) decreased all of the parameters of Ca^{2+} transient and contractile motion except the decay of Ca^{2+} transient (Fig. 3C and D). As shown in the bar charts in Fig. 3C and D, verapamil altered the Ca^{2+} transient amplitude, upstroke, decay and FWHM with 63, 78, 97 and 66%, respectively, while ADD, MCS, MRS and CRD with 52, 62, 63 and 66%, respectively. These results suggested that the contractile parameters of hiPS-CMs correspond to the intracellular Ca^{2+} status.

3.2. Correlation between the FP and the contractile motion of hiPS-CMs

We next performed a simultaneous recording of the contractile motion and FP using a hiPS-CM monolayer cultured in a MEA dish. To accurately evaluate the relationship between the motion and the FP of hiPS-CMs, the motion vectors were calculated from the hiPS-CMs that were located close to the vicinity of the electrode used for FP data collection. The yellow-squared area (150 × 150 μm) in Fig. 4A represents an example of the region that was used for evaluating contractile motion. Fig. 4B is an enlarged image, in which the calculated motion vectors (fine white bars) are overlaid on the image of the yellow-squared region shown in Fig. 4A. The MCS was ~10 to ~20 μm/s in normal culture conditions (e.g., 37 °C, 5% CO_2 and ~100% humidity) in the absence of any drugs. The simultaneously measured FP exhibited a typical waveform that had a sharp initial negative deflection, which is supposedly correlated with the inward Na^+ current. This is followed by a broad negative deflection (FP_{slow}) and a terminal positive deflection, which is supposedly correlated with the inward Ca^{2+} and outward K^+ currents, respectively [55–58]. As seen in the waveforms presented in Fig. 4C, D and E, several features of the relationship between the motion and the FP of hiPS-CMs were identifiable. These included 1) the CRD was longer than the FPD. The end of the FPD was previously defined as either the peak of the positive deflection [6,54,55,59] or the point where the positive deflection returns to the baseline [60]. The former end-point appears to be correlated with the upstroke of relaxation motion, while the latter end-point appears to be correlated with the peak of relaxation

motion. However, determination of an accurate end-point of FP proved difficult to establish. Other observed features included 2) the onset of the contraction motion follows the occurrence of the Na^+ current peak of the FP (see Fig. 4E), and 3) the position of FP_{slow} occurs with the contraction. The relationships between the motion profiles and the FP for the hiPS-CM described in 1) and 2) were also found in neonatal rat CMs (Supplementary Fig. 2). However, the point 3) was not observed in rats. In the neonatal rat CMs, the entire FP_{slow} was localized within the contraction motion and the broad positive deflection of the FP positions near the end of contraction motion (Supplementary Fig. 2B).

3.3. Correlation between the FP and the contractile motion of hiPS-CMs in the presence of drugs

To determine the correspondence between the contractile motion of the hiPS-CMs and the electrophysiological behavior obtained by the MEA technique, we examined various drugs that are known to inhibit Na^+, K^+ and Ca^{2+} channels.

3.3.1. The effects of a Na^+ channel blocker, tetrodotoxin (TTX)

It has been reported that Na^+ channel blockers decreased the amplitude and slope of the initial negative spike of FP waveform of CM

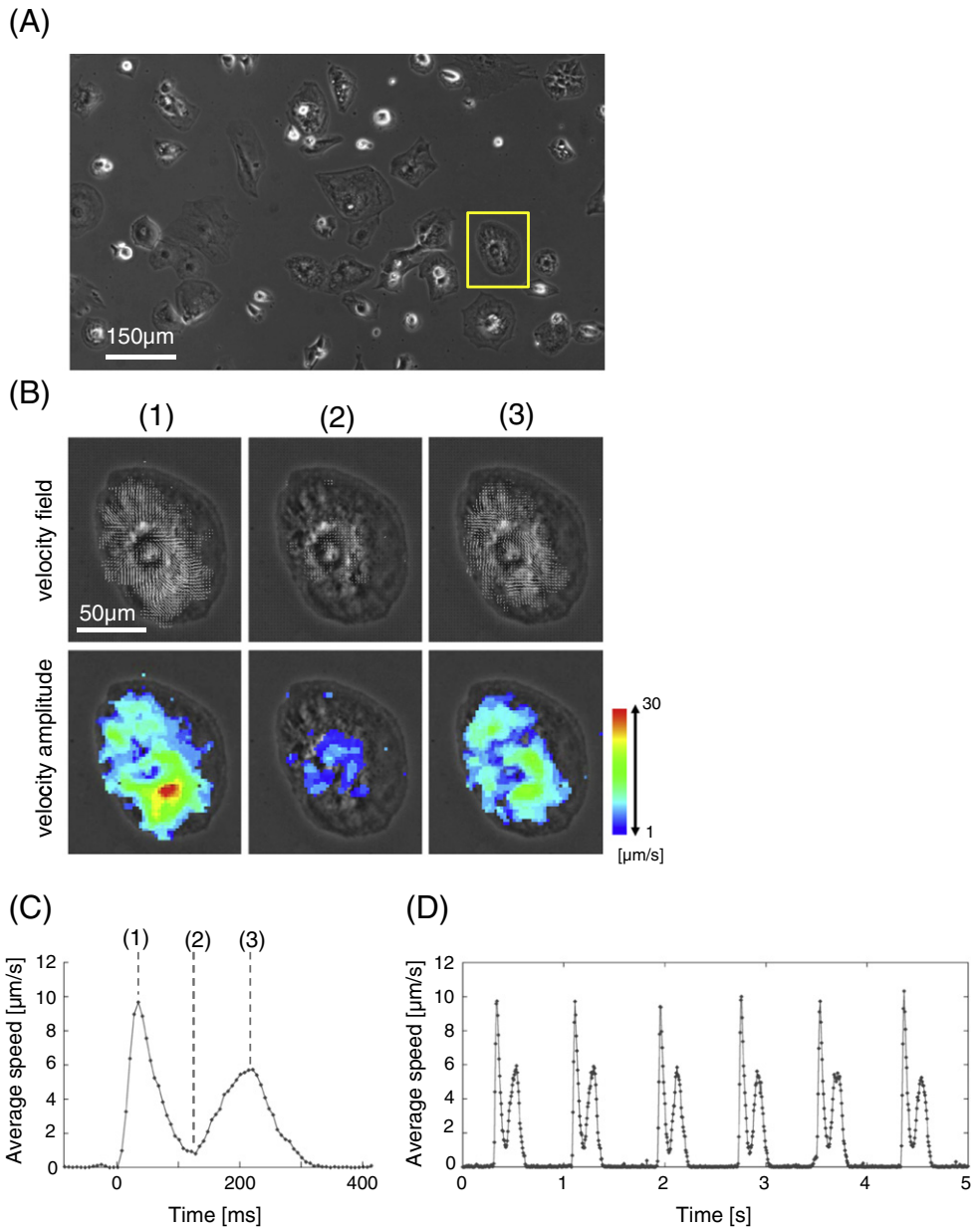

Fig. 1. Motion vectors detected during the contraction and relaxation process of a single hiPS-CM. (A) Example of a phase-contrast image of sparsely plated hiPS-CMs on a collagen-coated polystyrene dish, which was captured using a 10× objective. (B) Contractile motion of the hiPS-CM in the yellow-squared region in (A) was detected using motion vector analysis. In the upper panels, motion vectors show the velocity field at contraction (1), at the end of contraction (2) and at the relaxation (3). Bottom panels show the visualized amplitude of the velocity field in a heat-map style that corresponds to the upper panels. (C) Example of a motion waveform representing contraction and relaxation peaks, calculated with the single hiPS-CM shown in (B). Points (1)–(3) correspond to the same time points in the picture in part (B). (D) The train of motion waveform calculated with the single hiPS-CM shown in (B). (E) Schematics of a motion waveform of CM contraction–relaxation obtained with motion vector analysis. a–c in (E) represent contractile parameters evaluated in the present study, a: maximum contraction speed (MCS), b: maximum relaxation speed (MRS), c: average deformation distance (ADD) and d: contraction–relaxation duration (CRD). (F)–(J) show the summaries of contractile parameters and cell-area of single hiPS-CMs ($n = 40$), evaluated with motion vector analysis. Bars in (F)–(J) represent the average values for each plot. (K) Cell-area dependence of maximum contraction and relaxation speed (MCS and MRS). MCS and MRS were assessed from single hiPS-CMs ($n = 40$) and were plotted against their 2D area. Solid and dotted lines represent linear regression for MCS (black dots) and MRS (gray dots), respectively. (L) Correlation between CRD and the beating rate of single hiPS-CMs ($n = 40$).

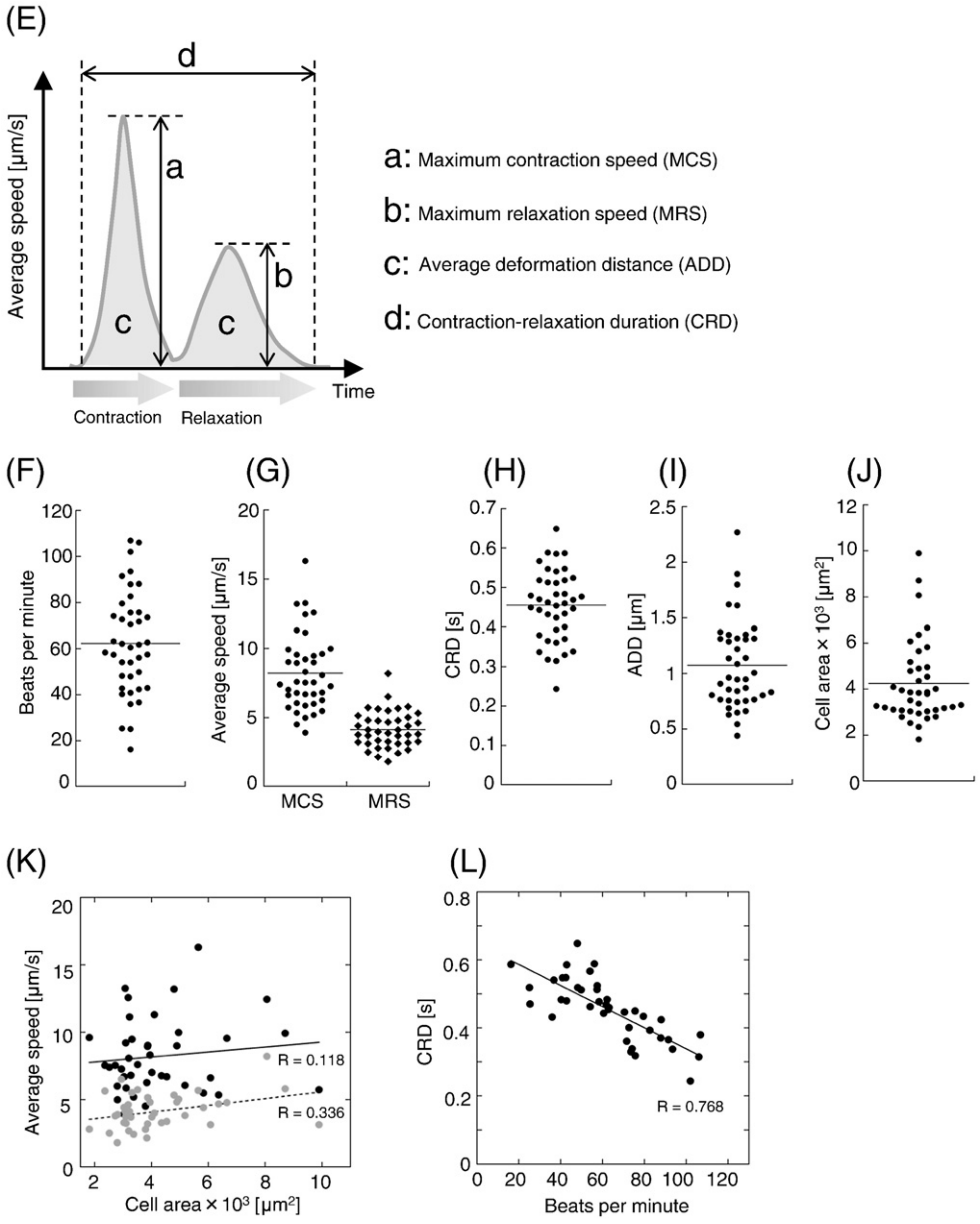

Fig. 1 (*continued*).

cultures [55,58,61]. To confirm the correspondence of these effects on the contractile behaviors of hiPS-CMs, we simultaneously recorded FP and motion of hiPS-CMs in the presence of 0–30 μM of TTX (Fig. 5A). Enlargement of the onset region of Fig. 5A is shown in Fig. 5B. The FP duration from the onset of the positive spike to the peak of the negative spike was significantly prolonged to 161% and 212% of the control at 9 and 30 μM of TTX, respectively, while the FPD measured as the duration between the initial negative peak and the peak of positive deflection increased to 106% and 110% of the control at the same concentrations. Along with the delay of the spikes, the Na^+ peak of FP exhibited broadening and a decrease in the peak slope. The contraction motion also exhibited a delay in the onset and peak position. As shown in Fig. 5C, the durations from the onset of the positive FP spike to the peak of the negative FP spike were linearly correlated with the durations from the onset of the positive FP spike to the onset of the contraction motion peak ($R = 0.856$). Although there was a progressive decrease in the beating rate in accordance with increasing TTX concentrations (Fig. 5G), no major increases in the FPD or CRD were observed (Fig. 5D and G). While the MRS was nearly unaffected, there was a significant decrease in the MCS (Fig. 5E). Despite this major decrease in the MCS, there was no significant alteration in the ADD (Fig. 5F).

3.3.2. The effects of a K^+ channel blocker, E-4031

A K^+ channel (I_{Kr}) blocker, E-4031, prolonged FPD of hiPS-CMs depending on the concentration (Fig. 6A), which is in line with previous reports [54,62]. The motion profile exhibited a prolongation of CRD, with a significant decrease in MRS (Fig. 6A). FPD and CRD showed a linear relationship in the presence of 0–50 nM E-4031 (Fig. 6B) with a correlation coefficient of $R = 0.915$. The slope of the linear regression was 1.362 (FPD/CRD). In the presence of 100 nM E-4031, the hiPS-CMs exhibited an EAD-like FP profile (Fig. 6A and C), i.e., there was an occurrence of negative deflection prior to the positive deflection. Since it was difficult to define the peak point of positive deflection, associated with K^+ current, or FPD in FP waveforms with EAD, we eliminated the data with EAD-like waveform from the evaluation of the CRD–FPD correlation (Fig. 6B). As shown in Fig. 6A and C, the motion profile also exhibited an irregular relaxation pattern that corresponded to the EAD-like FP waveform. This indicates that the speed of the relaxation

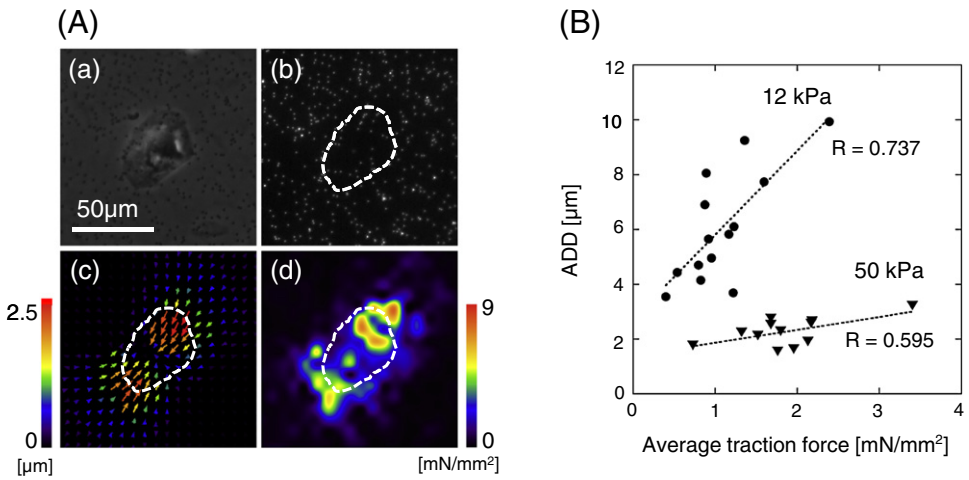

Fig. 2. (A) Parts (a) and (b) show the phase-contrast and fluorescent images of the hiPS-CM and the substrate with fluorescence beads (1 μm diameter), respectively. Part (c) is an example of a displacement field image of fluorescence beads calculated by the particle image velocimetry (PIV) algorithm. Part (d) shows an example of a traction force field image calculated using the PIV result from part (c) by the Fourier transform traction cytometry (FTTC) method. (B) Correlation between ADD and the normalized traction force (at 12 kPa (●) and 50 kPa (▼)) estimated with the FTTC algorithm. Bar in (a) represent 50 μm. The color scales for (c) and (d) are as indicated beside each of the figures.

decreased or almost momentarily stopped at the point of the negative deflection in the FP (see also Supplementary Movies 1 and 2). In the presence of 100 nM E-4031, there was a major decrease in the contractile parameters, MCS, MRS, ADD and the beating rate (Fig. 6E–G).

3.3.3. The effects of a Ca^{2+} channel blocker, verapamil

Fig. 7A shows the alterations in the motion and FP profiles of the hiPS-CMs in accordance with the verapamil concentration (0, 90, 150 nM). Increasing the verapamil concentration caused a progressive decrease in both the FPD and CRD that was well correlated with the correlation coefficient (R = 0.970) (Fig. 7B). The slope of the linear regression was found to be 0.633 (FPD/CRD). Since verapamil has an L-type Ca^{2+}-channel inhibiting effect, increasing verapamil concentration led to a decrease in FP_{slow} (Fig. 7A). Addition of verapamil also caused MCS to become smaller. There was a good correlation between the amplitudes of FP_{slow} and MCS, when these parameters were evaluated as a percent of the control, with a correlation coefficient of 0.921 (Fig. 7C). Increasing verapamil concentration also caused the MRS as well as ADD to decrease (Fig. 7C and D), and the beating rate to increase (Fig. 7E).

3.3.4. The effects of the positive inotropic reagent, isoproterenol

Fig. 8A shows the simultaneously measured motion and FP profile at isoproterenol concentrations of 0, 1, and 10 μM. With increasing isoproterenol concentrations, the CRD and FPD progressively shortened (Fig. 8A), with a good correlation observed (R = 0.943) (Fig. 8B). The slope of the linear regression was found to be 0.737 (FPD/CRD). For the motion profile, there were increases in the MCS, MRS, ADD as well as the beating rate, all depending on isoproterenol concentrations (Fig. 8C and D). These results suggest that the inotropic, lusitropic and chronotropic effects of isoproterenol can be detected with the motion of hiPS-CM monolayer.

3.4. Variability in contractile data

To test the possibility that contractile parameters of hiPS-CMs detected with the motion vector analysis is critically influenced by the heterogeneity in monolayer preparation, we evaluated the regional variability in MCS and MRS. MCS and MRS were obtained from motion data, and are summarized in Supplementary Fig. 3A and B. The average values of MCS and MRS under control conditions varied from 8 to 15 μm/s and from 4 to 10 μm/s, respectively, and were dependent on the regions of monolayer. These values were altered by the addition of a Ca^{2+} channel blocker, verapamil, which had a negative inotropic effect and similar variability to that of the control. By expressing these values to a percent of the control, we found that each value converged to a similar percentage value (Supplementary Fig. 3A and B). This indicates that the relative values of contractile parameters are significantly less dependent on the region in the preparation.

4. Discussion

The present study aimed to evaluate contractile characteristics and the correlation between contractile motion and electrical properties of hiPS-CM monolayer by using video microscopy, Ca^{2+} transient imaging, traction force microscopy and FP measurement. High resolution motion vector analysis could detect contractile characteristics of hiPS-CMs, i.e., MCS, MRS, ADD and CRD, quantitatively, and demonstrated the correspondence between contractile motion and FP. Motion data further provided complementary information against FP, by detecting the inotropic and lusitropic effects of an experimental drug, isoproterenol. The accessibility to information about relaxation process, or lusitropism, is considered to be one of the advantages of this imaging approach. Recently, there has been increasing attention to the diastolic dysfunction characterized by decreased relaxation velocity and prolonged relaxation and its applicability to common cardiac pathologies, such as ischemic heart diseases and hypertensive heart diseases, and to rare genetic heart diseases, such as DCM [63,64]. The imaging approach could potentially be used to target and analyze hiPS-CMs derived from such diseases.

4.1. Contractile characteristics of hiPS-CMs detected with video microscopy

It has been previously reported that alterations in hiPS-CM area depend on substrate stiffness [26] or cell density [65]. We examined the cell area and the contractile parameters (MCS and MRS) of hiPS-CMs ($n = 40$) and observed no significant dependence of MCS and MRS on cell area. Since in our current study, we sparsely plated hiPS-CMs in order to extract single cell information, average cell area became relatively larger (4244 ± 279 μm^2, $n = 40$) than that recently reported (1654 μm^2, $n = 22$) for hiPS-CMs (iCell CMs) that were plated in a monolayer form with a density of 22,500 cells in the well of a 96-well multiplate [65]. As seen in Fig. 1, the hiPS-CMs attached to the substrate exhibited a heterogeneous shape and their contractile motion often

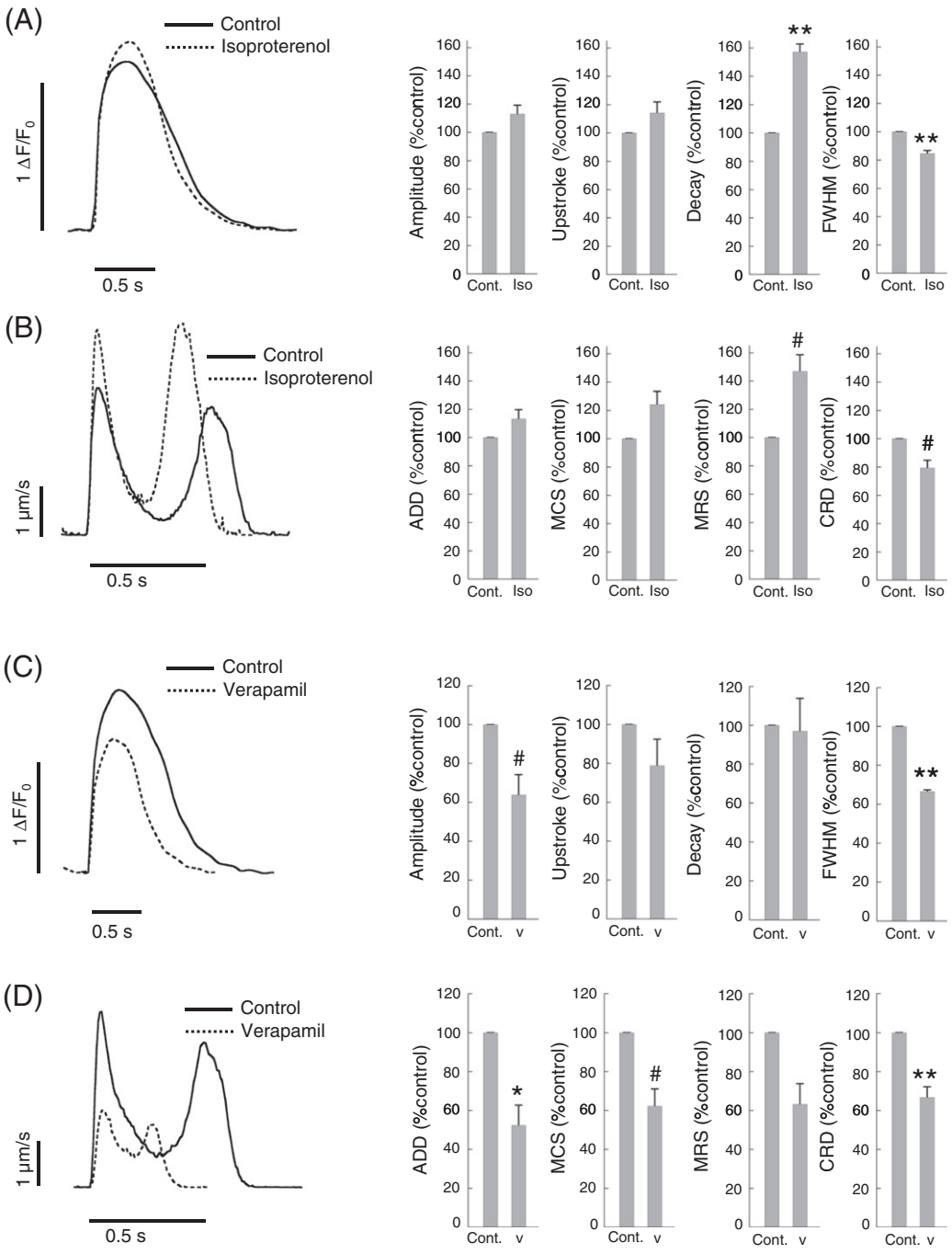

Fig. 3. (A) and (B) show the example profiles of the Ca^{2+} transient and motion waveform of hiPS-CMs, respectively, in the presence of 100 nM isoproterenol. (C) and (D) also show the example profiles of the Ca^{2+} transient and motion waveform of hiPS-CMs, respectively, in the presence of 100 nM verapamil. The bar charts in (A) and (C) represent the drug-induced change in amplitude, maximum upstroke, maximum decay and FWHM of the Ca^{2+}-transient. In (B) and (D), change rate of the contractile parameters, ADD, MCS, MRS and CRD, were also shown in bar charts. The Ca^{2+} transient and motion data were obtained independently. In all the bar charts, values are means ± SE and are expressed as percentage of control.

occurred locally in the cell body. Therefore, it should not be surprising that the average velocity of hiPS-CMs would not correlate well with their cell area. It has been reported that hiPS-CMs cultured for prolonged period, e.g., 90 days, exhibited rod-shaped morphology [66] like adult CMs filled with an aligned sarcomere structure [67]. Those morphologically matured hiPS-CMs, which were not tested in this study, could represent area dependence of contractile speed.

The image-based edge-detection technique has been the method of choice for measuring the shortening of the length of the whole cell body or sarcomere of the rod-shaped adult CMs in order to estimate the force development [34,41–43]. In contrast, TFM has been utilized to assess the contractility of cultured CMs that exhibit an amorphous shape [26,68,69]. With TFM, the traction force of the cells can be estimated based on the deformation of the substrate, which is detected by the displacement of fluorescent beads embedded in the substrate, and on the elastic modulus of the substrate [70]. In our study, we examined the correlation between the force development and cellular deformation (ADD) of the hiPS-CMs. As shown in Fig. 2B, ADD appeared to be correlated with the force development on the substrates (12 kPa and 50 kPa). Phase-contrast microscopy observes

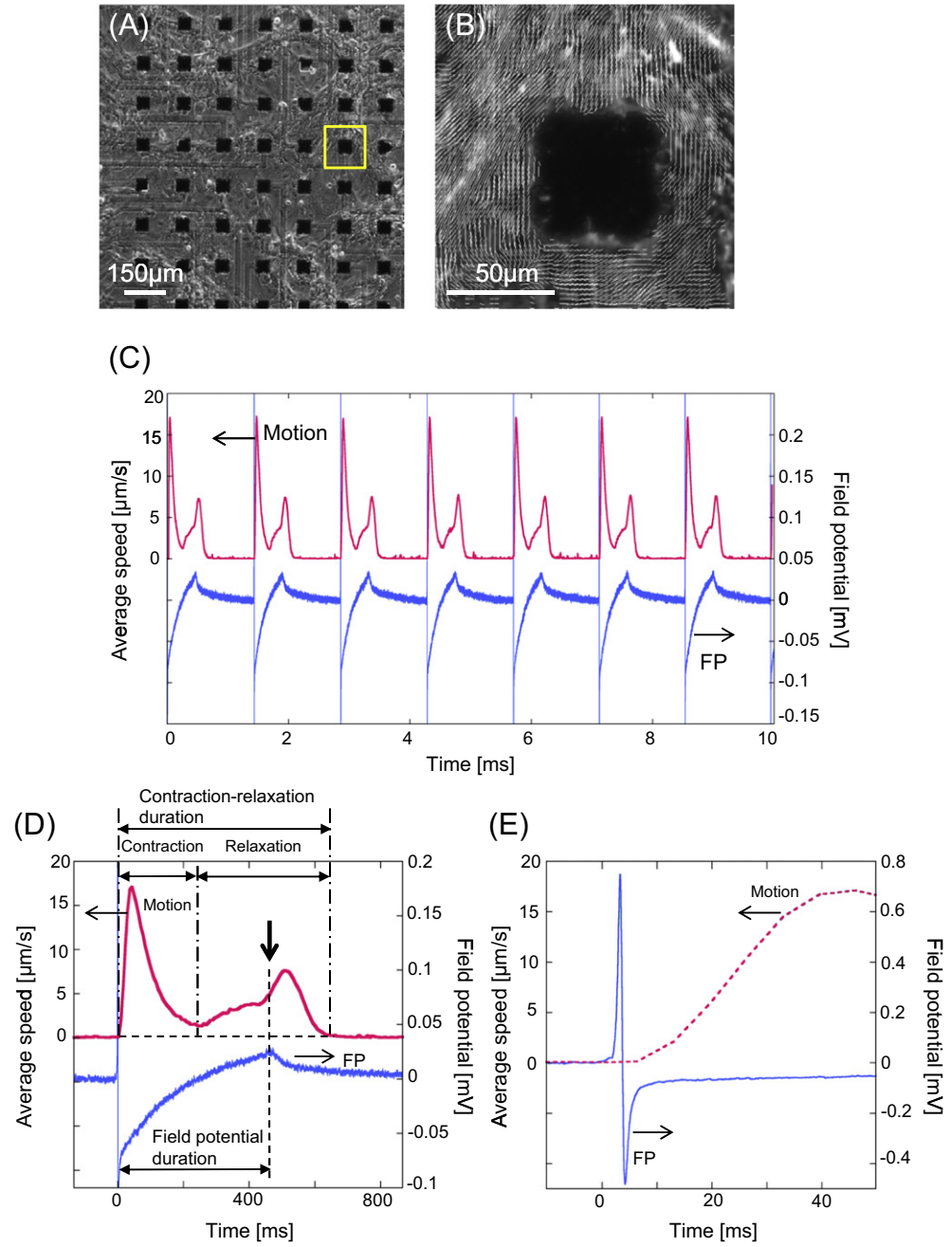

Fig. 4. (A) Phase-contrast image of the hiPS-CM monolayer prepared on the MEA probe. (B) The enlarged velocity field image for the yellow-square region is shown in (A), which shows the motion vectors as fine white lines. (C) Example profile of simultaneously measured hiPS-CM motion and FP. The motion data were evaluated from the region in close vicinity to the electrode (e.g., the yellow-square region in Fig. 4A) that was used for the FP data acquisition. (D) An enlarged single beat profile. The horizontal dashed line represents the baseline of the average velocity (0 μm/s). The vertical dot–dashed lines illustrate the durations of contraction and relaxation of the motion profile. The vertical dashed line with the arrow shows the peak position of positive deflection of the FP. (E) Magnified figure of the onset region of the FP and the motion shown in (D). Time zero corresponds to the onset of the positive FP spike.

overall deformation/displacement of hiPS-CMs during the contraction–relaxation process, including passively moving cellular boundaries and intracellular compartments or organelle. Our present results suggested that the average cellular deformation, ADD, detected by phase-contrast microscopy and motion vector analysis represents the extent of the force development of the hiPS-CMs on the substrates. As long as intra- and extra-cellular elastic properties (e.g., adhesion between hiPS-CMs and substrate) of hiPS-CMs are not altered during the measurement, ADD can be a surrogate marker for the force development of hiPS-CMs.

Isoproterenol and verapamil have been shown to alter the amplitude of the fluorescence peak of the Ca^{2+} transient in iPS-CMs [19]. In our current study, we examined whether the Ca^{2+} transient of hiPS-CMs was correlated with motion behavior in the presence of isoproterenol and verapamil. Responses of the Ca^{2+} transient in hiPS-CMs observed against isoproterenol included an increase in the amplitude, upstroke and decay (Fig. 3A). Interestingly, the maximum decay of the Ca^{2+} transient in the presence of isoproterenol showed a higher increased rate (~160% increase from control) compared to that of maximum upstroke, which is consistent with greater increases in MRS than in MCS of motion

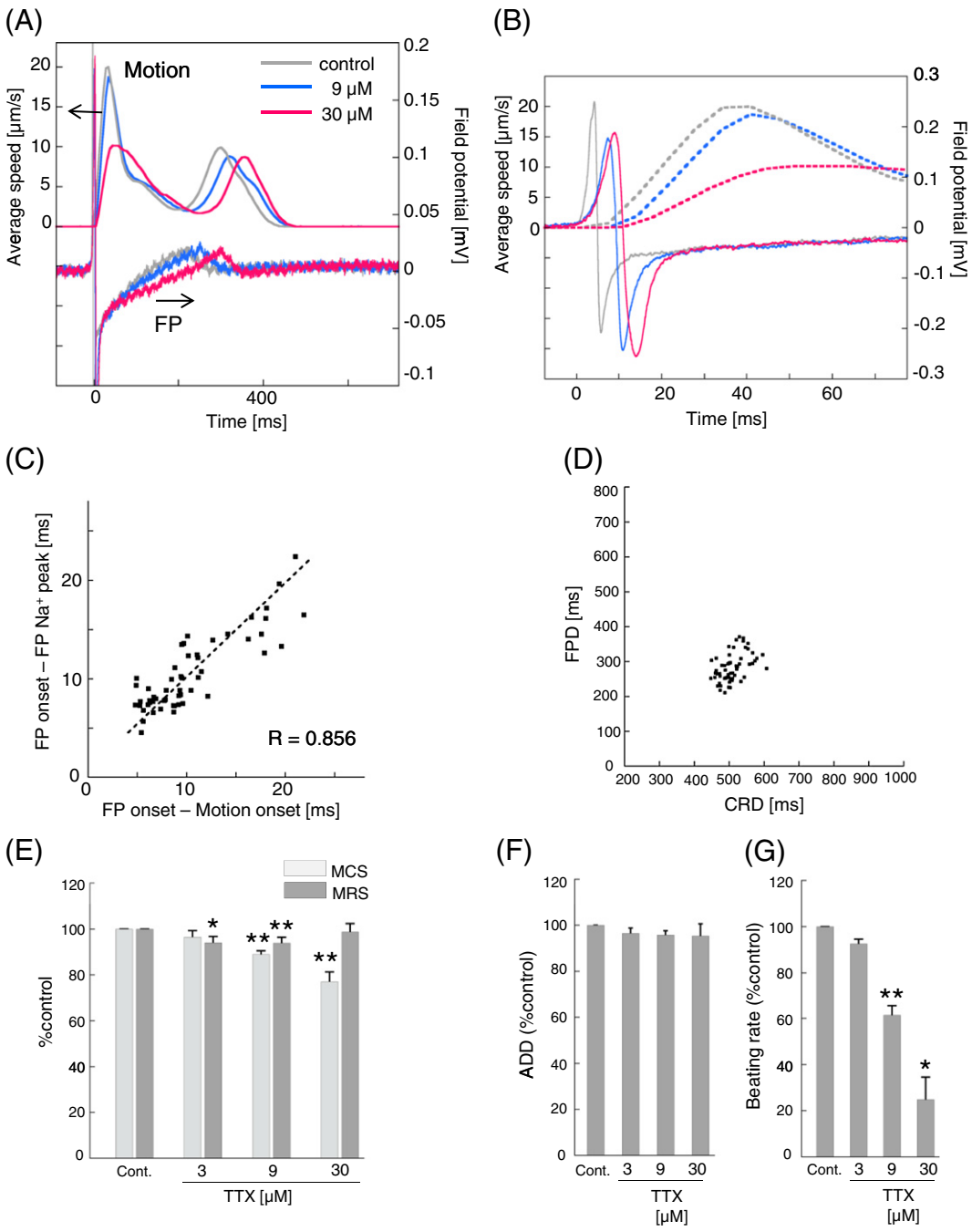

Fig. 5. Contractile and FP responses of the hiPS-CM to tetrodotoxin (TTX). (A) Example of motion and FP profiles of the hiPS-CMs simultaneously measured in the presence of 0, 9, and 30 μM of TTX. (B) Correlation between the CRD and FPD obtained with varied concentrations of TTX (0–30 μM). (C) Enlargement of the onset region of the FP and motion profiles. (D) Correlation of the FP onset-to-FP Na + peak and FP onset-to-motion onset with varied concentrations of TTX (0–30 μM). (E) The normalized change of the MCS and MRS with 0–30 μM of TTX. (F) and (G) show the normalized change of the ADD and beating rate in accordance with the 0–30 μM TTX concentration, respectively. Data were obtained from 15 electrodes with 3 independent preparations and are expressed as means ± SE. $^{*}p < 0.05$; $^{**}p < 0.01$ and $^{\#}p < 0.10$ compared with the control.

response. Verapamil decreased all of the parameters of the Ca^{2+} transient in hiPS-CMs (Fig. 3C, D). This is attributed to verapamil's blockage of the L-type Ca^{2+} channel, which is supported by the FP data shown in Fig. 7C. Thus, decreased contraction and relaxation speeds as well as ADD of hiPS-CMs in the presence of verapamil (Fig. 7D and E) can also be attributed to decreased cytoplasmic Ca^{2+} concentration associated with the Ca^{2+}-induced Ca^{2+} release mechanism. Taken together, these data suggest that the cellular deformation in the hiPS-CM monolayer shows a correspondence to the cytoplasmic Ca^{2+} status, observed with a common fluorescence indicator.

4.2. Correlation between the FP and contractile motion of the hiPS-CMs

Our simultaneous measurements of motion and FP confirmed the following correlations under non-arrhythmic conditions: 1) CRD is longer than the FPD; 2) the onset of contraction motion follows the

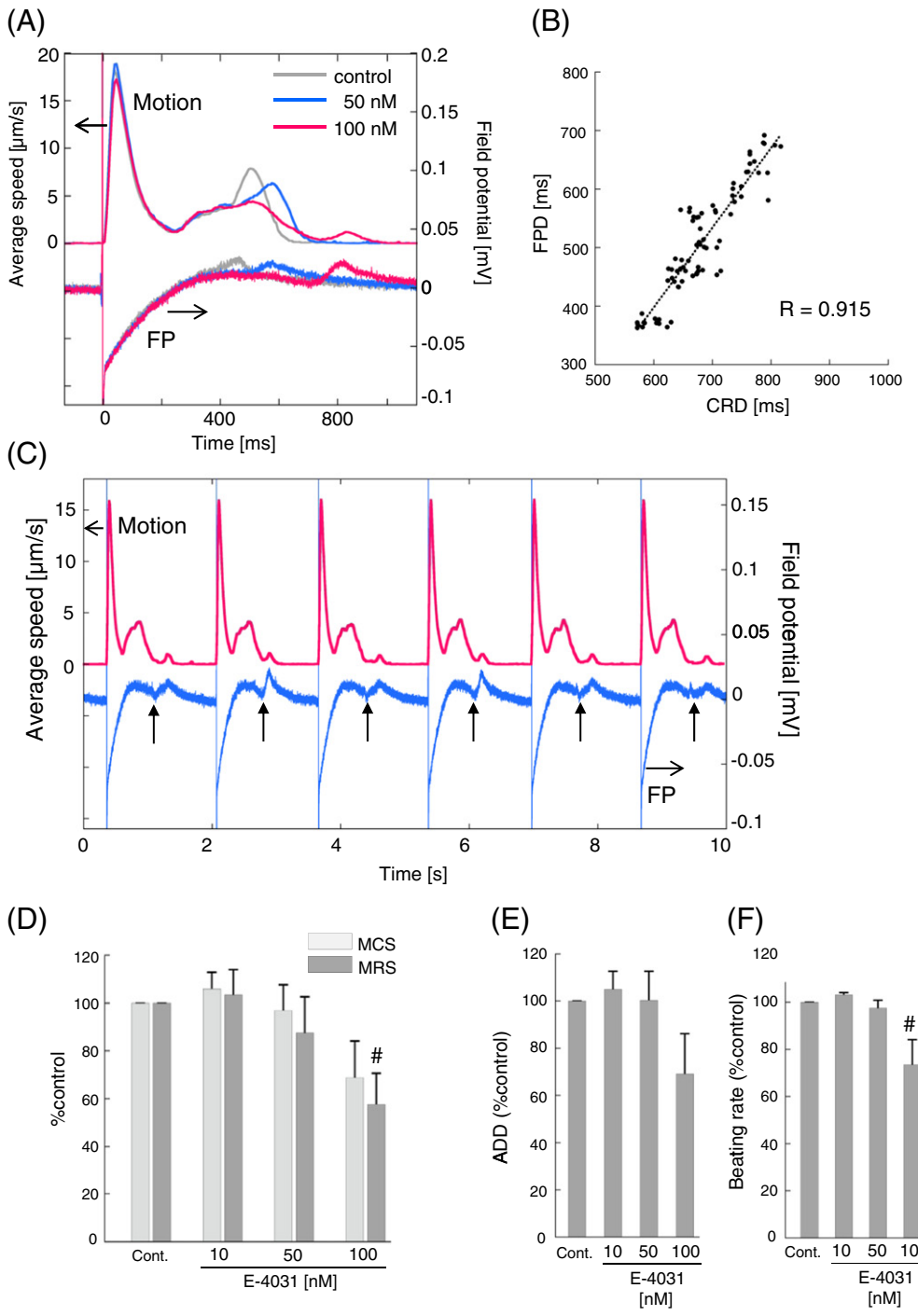

Fig. 6. Contractile and FP responses of the hiPS-CM to E-4031. (A) Example of the motion and FP profiles of the hiPS-CMs simultaneously measured in the presence of 0, 50, and 100 nM of E-4031. (B) Correlation of the CRD and FPD obtained when using varied concentrations of E-4031 (0–~50 nM). Dotted line is a linear regression fitted to the data with R = 0.915 and the slope = 1.362 (FPD/CRD). (C) Relationship between the motion and FP in the presence of 100 nM E-4031. Arrows in (C) indicate the points of the negative deflection in the FP waveform during the relaxation process. Pauses in the relaxation motion corresponded to the negative FP deflections (see also Supplementary Movie 2). (D) Normalized change of the MCS and MRS with 0–100 nM of E-4031. (E) and (F) show the normalized change of the ADD and beating rate in accordance with the 0–100 nM E-4031 concentration changes. Data were obtained from 7 independent preparations of the hiPS-CM monolayer. In (D)–(F), values are expressed as means ± SE. $^{*}p < 0.05$; $^{**}p < 0.01$ and $^{\#}p < 0.10$ compared with the control.

occurrence of the Na^{+} current peak of FP; and 3) the position of the negative broad deflection in FP occurs with the contraction. We also observed relationships 1) and 2), but not 3), in neonatal rat CMs. It is noteworthy that while we found the motion profile of hiPS-CMs exhibited a certain amount of displacement (velocity) at the minimum point between contraction and relaxation peak (Figs. 1 and 4), neonatal rat CMs showed almost no displacement (velocity) at the same position (Supplementary Fig. 2). While this observation for the hiPS-CMs appeared to be derived from the lack of any synchronized motion at the end of the contraction, the precise mechanism for this phenomenon remains unclear. Differences in the contraction motion between hiPS-CMs and rat CMs may reflect the presence and absence of the plateau phase

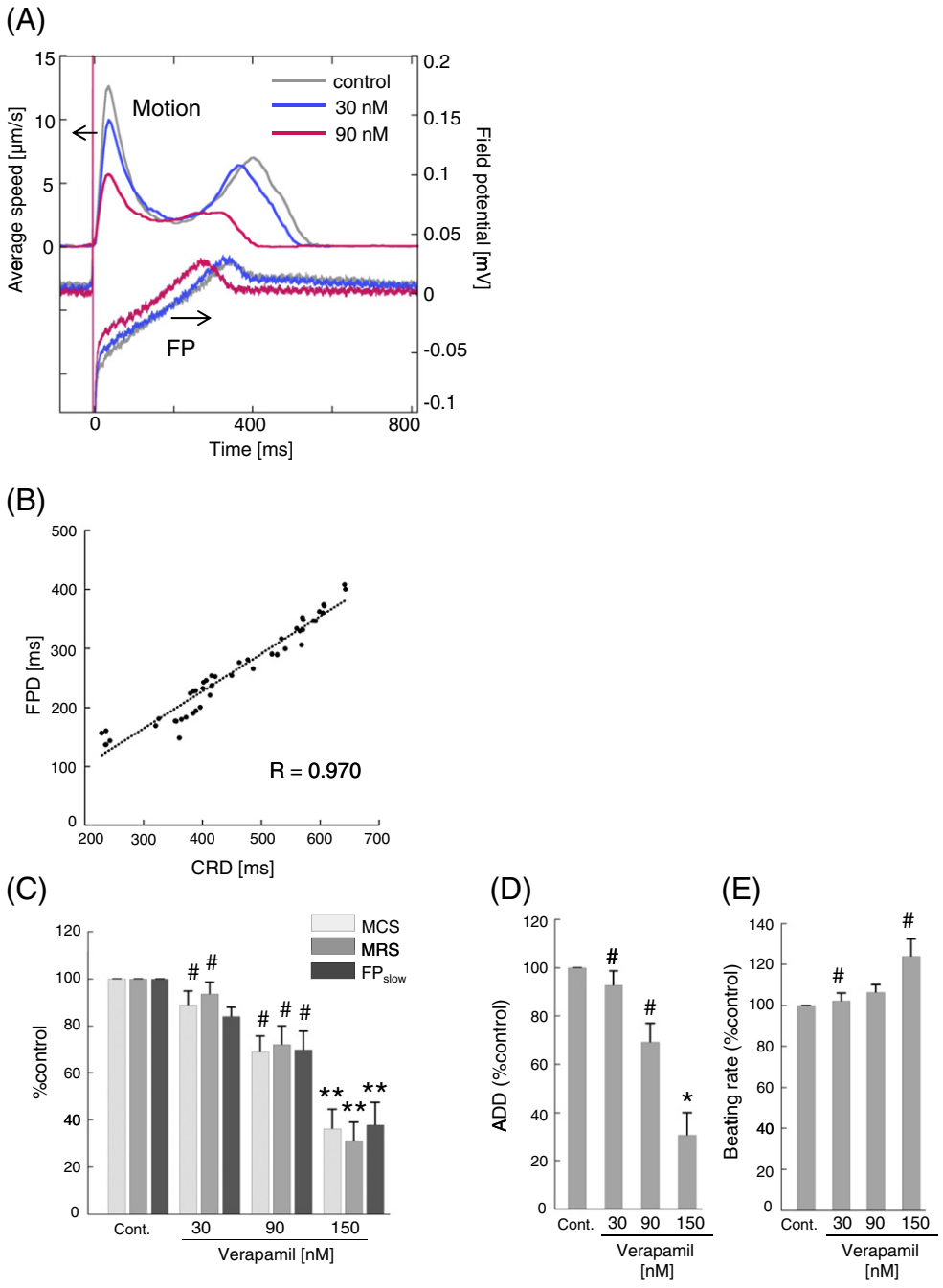

Fig. 7. Contractile and FP responses of the hiPS-CM to verapamil. (A) Example of the motion and FP profiles of the hiPS-CMs simultaneously measured in the presence of 0, 90, and 150 nM of verapamil. (B) Correlation of the CRD and FPD obtained with varied concentrations of verapamil (0–270 nM). Dotted line is a linear regression fitted to the data with R = 0.970 and the slope = 0.633 (FPD/CRD). (C) Change of the rate of the MCS, MRS and the amplitude of FP_{slow}. The amplitude of FP_{slow} was evaluated by averaging the FP value for 6 ms (between 3 ms before and 3 ms after the point of the peak of the contraction motion). (E) and (F) show the normalized change of ADD and beating rate, respectively. Data were obtained from 5 to 8 independent preparations of the hiPS-CM monolayer. In (C)–(E), values are expressed as means ± SE. $^{*}p < 0.05$; $^{**}p < 0.01$ and $^{\#}p < 0.10$ compared with the control.

of their action potential [71–73]. Alternatively, it may be relevant to the immaturity of hiPS-CM sarcoplasmic reticulum, as suggested for hES-CMs [28,29].

We performed a simultaneous measurement of motion and FP from the hiPS-CM monolayer in the presence of TTX, E-4031, verapamil and isoproterenol. The experiments revealed a linear relationship between the CRD and FPD in the presence of E-4031 (10–50 nM), verapamil (30–150 nM) and isoproterenol (0.1–10 μM). Although the slope of the CRD–FPD relationship was suggested to be different in each drug, the present results suggested that the CRD can be a surrogate of the FPD in non-arrhythmic conditions. However, it should be noted that the lower time resolution of motion vector (~6 ms data interval) compared to that of FP (0.05 ms data interval) could be of concern.

Due to the blockage of I_{Kr} with E-4031, it is reasonable to assume that the relaxation speed was decreased at the point where the K^+ current occurred. With regard to the duration, even in the presence of 10–50 nM E-4031, the profile of CRD–FPD correlation appeared to be well correlated with the correlation coefficient of R = 0.915, and the slope of the linear regression was 1.362 (FPD/CRD) (Fig. 6B). This slope value appeared to be significantly larger than the case of verapamil (0.633 (FPD/CRD)) shown in Fig. 7B. This may be relevant to the abnormalities in electro-mechanical relationship reported for the Torsade

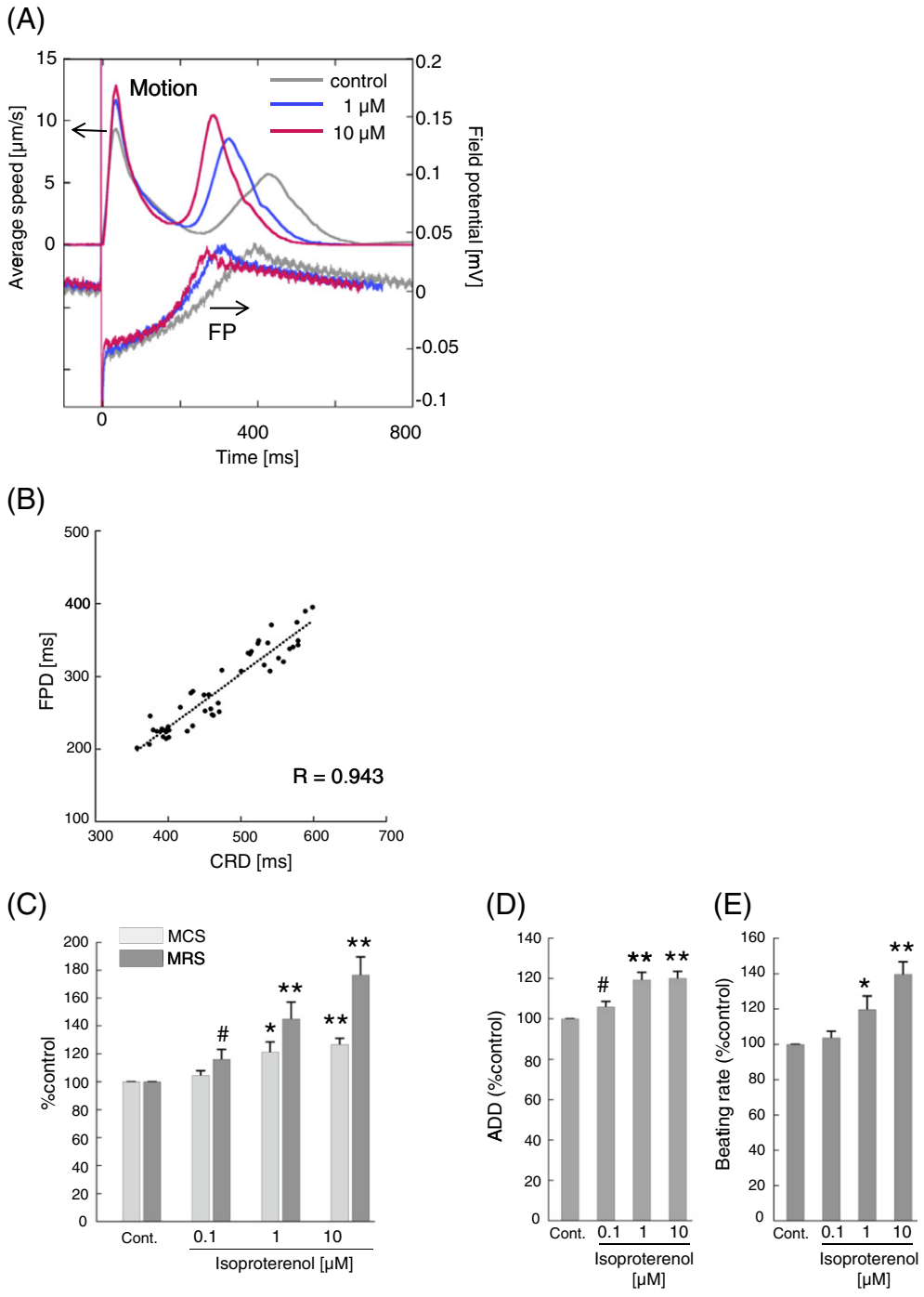

Fig. 8. Contractile and FP responses of the hiPS-CM to isoproterenol. (A) Example of the motion and FP profiles of the hiPS-CMs simultaneously measured in the presence of 0, 1, and 10 μM of isoproterenol. (B) Correlation of the CRD and FPD obtained when using various concentrations of isoproterenol (0–10 μM). Dotted line is a linear regression fitted to the data with R = 0.943 and the slope = 0.738 (FPD/CRD). (C) Normalized change of the MCS and MRS with 0–10 μM of isoproterenol. (D) and (E) show the normalized change of the ADD and beating rate, respectively. Data were evaluated from 7 independent preparations of the hiPS-CM monolayer. In (C)–(E), values are expressed as means ± SE. $^{*}p < 0.05$; $^{**}p < 0.01$ and $^{\#}p < 0.10$ compared with the control.

de Pointes-genic drugs [74–76]. However, to determine the precise relation between FPD and CRD, it is necessary to determine FPD accurately even when the extensive broadening occurred and to consider the beating rate, which is beyond the scope of the present paper and is needed to be examined in a further study. In the presence of 50–100 nM E-4031, the EAD-like negative deflection in the FP waveform was observed. EADs are caused by the re-activation of the inactivated L-type Ca^{2+} current or the inactivated voltage-dependent Na^{+} current, with the latter associated with the activation of the forward cycle of the Na^{+}/Ca^{2+} exchanger and the resultant Ca^{2+} influx. Thus, it is conceivable that the EAD is associated with the transient increase in the intracellular Ca^{2+} concentration, which leads to a reduction of the relaxation motion speed before completion of the relaxation process, thereby resulting in the appearance of another motion peak at the end of relaxation (Fig. 6C). As recognized in the video images of hiPS-CMs in the presence of 100 nM E-4031 (Supplementary video 2), however, such additional single peaks were a part of relaxation motion, not of an independent contraction–relaxation motion. After the occurrence of this type of two-step relaxation motion, triggered activity followed by arrhythmic beating were often observed (data not

shown). EAD-induced contraction, or triggered activity, was also reported using a video edge-detection system for hiPS-CMs in the presence of E-4031 [77]. The occurrence of another motion peak at the end of relaxation could be a potential marker for the early detection of EAD.

Verapamil increased the beating rate of hiPS-CM (Fig. 7E). Although this effect would not be expected to occur based on verapamil's mechanism of action and previous clinical findings [78–80], verapamil has been reported to have a positive chronotropic effect on hES-CMs [54]. In accordance with the concentration of verapamil used in the current study, decreases were observed in MCS and in the amplitude of FP_{slow}. FP_{slow} was also decreased under Ca^{2+}-free condition in embryonic mouse CMs and was suggested to reflect the current of L-type Ca^{2+} channel [55]. Although FP_{slow} does not solely represent the extent of the Ca^{2+} current, their relative values (% of control) were in good agreement with those of the MCS.

Isoproterenol was also observed to increase beating rate, MCS, MRS and ADD. The increasing rate of maximum velocity was greater during relaxation (176% at 10 μM, $n = 7$) versus that during contraction (126% at 10 μM, $n = 7$) (Fig. 8C). Although the precise reason for these findings is currently unknown, Turnbull et al. described the negligible inotropic response of hES-CMs against isoproterenol and pointed out the immaturity of the sarcoplasmic reticulum of the hES-CMs [29]. Pillekampt et al. also reported that isoproterenol significantly induced positive chronotropy and lusitropy but not inotropy in early hES-CMs [28]. The mechanism underlying the hES-CMs findings in their study could be relevant to our current hiPS-CM observations. On the other hand, the FP profile showed no major alterations by the addition of isoproterenol with the exception of the shortening in FPD. Although the L-type Ca^{2+} channel is one of the targets of the isoproterenol action, alterations in FP_{slow} were not clearly detected with isoproterenol. This could be partly due to that negative deflection in FP does not solely reflect the L-type Ca^{2+} current, since the FP is an extracellular potential and not a cell membrane potential.

4.3. Variability in the contractile data

To some extent, the absolute values of MCS and MRS of hiPS-CMs depend on the monolayer region (Supplementary Fig. 3A). The reasons for this regional heterogeneity can be considered to be as follows: 1) the cell density may not be thoroughly homogeneous in the well, 2) the cell size and contractile characteristics have some variability, 3) the hiPS-CM monolayer contains a certain amount of non-cardiac (non-contracting) cells (~2%), and 4) the monolayer preparations contain a variety of shapes and types (atrial-, ventricular- and nodal-type) of hiPS-CMs. However, as long as we evaluate the contractile parameters from the same field of view in the monolayer and express the parameters using a relative value (i.e., % of the control), the inter-region variability of the contractile parameters should be fairly small (Supplementary Fig. 3B). It is possible that non-cardiac cells may have affected the contractile properties of our cultures because those cells move passively with lower motion speed than that of contracting hiPS-CMs. However, we assumed that they were present to a similar extent in all regions in the monolayer and hence should not have affected the validity of our results.

In conclusion, this study demonstrated that the contractile motion of 2D cultured hiPS-CMs, detected by a high-speed camera and motion vector analysis, quantitatively corresponded to their electrophysiological and functional behaviors under non-arrhythmic condition. Although the relationship between hiPS-CM motion and FP during excitation–contraction decoupling or proarrhythmic conditions is of great interest, it is not within the scope of this current paper and will need to be examined in a further study. The results of the present study will open up the possibilities of detecting cellular-level information on the electric and mechanical relationship of cultured CMs and will contribute to expand the applicability of hiPS-CMs in the field of cellular cardiology, drug screening and cardiac therapeutics.

Supplementary data to this article can be found online at http://dx.doi.org/10.1016/j.yjmcc.2014.09.010.

Disclosure Statement

T.H., T.K., S.K., E.M. and H.Y. are employed by Sony Corporation.

References

[1] Habib M, Caspi O, Gepstein L. Human embryonic stem cells for cardiomyogenesis. J Mol Cell Cardiol Oct 2008;45(4):462–74.
[2] Caspi O, Itzhaki I, Kehat I, Gepstein A, Arbel G, Huber I, et al. In vitro electrophysiological drug testing using human embryonic stem cell derived cardiomyocytes. Stem Cells Dev Jan–Feb 2009;18(1):161–72.
[3] Tanaka T, Tohyama S, Murata M, Nomura F, Kaneko T, Chen H, et al. In vitro pharmacologic testing using human induced pluripotent stem cell-derived cardiomyocytes. Biochem Biophys Res Commun Aug 7 2009;385(4):497–502.
[4] Guo L, Abrams RM, Babiarz JE, Cohen JD, Kameoka S, Sanders MJ, et al. Estimating the risk of drug-induced proarrhythmia using human induced pluripotent stem cell-derived cardiomyocytes. Toxicol Sci Sep 2011;123(1):281–9.
[5] Kadota S, Minami I, Morone N, Heuser JE, Agladze K, Nakatsuji N. Development of a reentrant arrhythmia model in human pluripotent stem cell-derived cardiac cell sheets. Eur Heart J Apr 2013;34(15):1147–56.
[6] Nakamura Y, Matsuo J, Miyamoto N, Ojima A, Ando K, Kanda Y, et al. Assessment of testing methods for drug-induced repolarization delay and arrhythmias in an iPS cell-derived cardiomyocyte sheet: multi-site validation study. J Pharmacol Sci 2014;124(4):494–501.
[7] Caspi O, Lesman A, Basevitch Y, Gepstein A, Arbel G, Habib IH, et al. Tissue engineering of vascularized cardiac muscle from human embryonic stem cells. Circ Res Feb 2 2007;100(2):263–72.
[8] Yoshida Y, Yamanaka S. iPS cells: a source of cardiac regeneration. J Mol Cell Cardiol Feb 2011;50(2):327–32.
[9] Kawamura M, Miyagawa S, Fukushima S, Saito A, Miki K, Ito E, et al. Enhanced survival of transplanted human induced pluripotent stem cell-derived cardiomyocytes by the combination of cell sheets with the pedicled omental flap technique in a porcine heart. Circulation Sep 10 2013;128(11 Suppl. 1):S87–94.
[10] Sawa Y, Miyagawa S. Present and future perspectives on cell sheet-based myocardial regeneration therapy. BioMed Res Int 2013;2013:583912.
[11] Matsuura K, Haraguchi Y, Shimizu T, Okano T. Cell sheet transplantation for heart tissue repair. J Control Release Aug 10 2013;169(3):336–40.
[12] Itzhaki I, Schiller J, Beyar R, Satin J, Gepstein L. Calcium handling in embryonic stem cell-derived cardiac myocytes: of mice and men. Ann N Y Acad Sci Oct 2006;1080:207–15.
[13] Satin J, Itzhaki I, Rapoport S, Schroder EA, Izu L, Arbel G, et al. Calcium handling in human embryonic stem cell-derived cardiomyocytes. Stem Cells Aug 2008;26(8):1961–72.
[14] Zwi L, Caspi O, Arbel G, Huber I, Gepstein A, Park IH, et al. Cardiomyocyte differentiation of human induced pluripotent stem cells. Circulation Oct 13 2009;120(15):1513–23.
[15] Itzhaki I, Rapoport S, Huber I, Mizrahi I, Zwi-Dantsis L, Arbel G, et al. Calcium handling in human induced pluripotent stem cell derived cardiomyocytes. PLoS One 2011;6(4):e18037.
[16] Lee YK, Ng KM, Lai WH, Chan YC, Lau YM, Lian Q, et al. Calcium homeostasis in human induced pluripotent stem cell-derived cardiomyocytes. Stem Cell Rev Nov 2011;7(4):976–86.
[17] Jonsson MK, Vos MA, Mirams GR, Duker G, Sartipy P, de Boer TP, et al. Application of human stem cell-derived cardiomyocytes in safety pharmacology requires caution beyond hERG. J Mol Cell Cardiol May 2012;52(5):998–1008.
[18] Zhang GQ, Wei H, Lu J, Wong P, Shim W. Identification and characterization of calcium sparks in cardiomyocytes derived from human induced pluripotent stem cells. PLoS One 2013;8(2):e55266.
[19] Sirenko O, Crittenden C, Callamaras N, Hesley J, Chen YW, Funes C, et al. Multiparameter in vitro assessment of compound effects on cardiomyocyte physiology using iPSC cells. J Biomol Screen Jan 2013;18(1):39–53.
[20] Navarrete EG, Liang P, Lan F, Sanchez-Freire V, Simmons C, Gong T, et al. Screening drug-induced arrhythmia events using human induced pluripotent stem cell-derived cardiomyocytes and low-impedance microelectrode arrays. Circulation Sep 10 2013;128(11 Suppl. 1):S3–S13.
[21] Xi J, Khalil M, Shishechian N, Hannes T, Pfannkuche K, Liang H, et al. Comparison of contractile behavior of native murine ventricular tissue and cardiomyocytes derived from embryonic or induced pluripotent stem cells. FASEB J Aug 2010;24(8):2739–51.
[22] Hansen A, Eder A, Bonstrup M, Flato M, Mewe M, Schaaf S, et al. Development of a drug screening platform based on engineered heart tissue. Circ Res Jul 9 2010;107(1):35–44.
[23] Liau B, Christoforou N, Leong KW, Bursac N. Pluripotent stem cell-derived cardiac tissue patch with advanced structure and function. Biomaterials Dec 2011;32(35):9180–7.
[24] Schaaf S, Shibamiya A, Mewe M, Eder A, Stohr A, Hirt MN, et al. Human engineered heart tissue as a versatile tool in basic research and preclinical toxicology. PLoS One 2011;6(10):e26397.

[25] Tulloch NL, Muskheli V, Razumova MV, Korte FS, Regnier M, Hauch KD, et al. Growth of engineered human myocardium with mechanical loading and vascular coculture. Circ Res Jun 24 2011;109(1):47–59.
[26] Hazeltine LB, Simmons CS, Salick MR, Lian X, Badur MG, Han W, et al. Effects of substrate mechanics on contractility of cardiomyocytes generated from human pluripotent stem cells. Int J Cell Biol 2012;2012:508294.
[27] Liu J, Sun N, Bruce MA, Wu JC, Butte MJ. Atomic force mechanobiology of pluripotent stem cell-derived cardiomyocytes. PLoS One 2012;7(5):e37559.
[28] Pillekamp F, Haustein M, Khalil M, Emmelheinz M, Nazzal R, Adelmann R, et al. Contractile properties of early human embryonic stem cell-derived cardiomyocytes: beta-adrenergic stimulation induces positive chronotropy and lusitropy but not inotropy. Stem Cells Dev Aug 10 2012;21(12):2111–21.
[29] Turnbull IC, Karakikes I, Serrao GW, Backeris P, Lee JJ, Xie C, et al. Advancing functional engineered cardiac tissues toward a preclinical model of human myocardium. FASEB J Feb 2014;28(2):644–54.
[30] Sun N, Yazawa M, Liu J, Han L, Sanchez-Freire V, Abilez OJ, et al. Patient-specific induced pluripotent stem cells as a model for familial dilated cardiomyopathy. Sci Transl Med Apr 18 2012;4(130):130ra47.
[31] Tameyasu T, Toyoki T, Sugi H. Nonsteady motion in unloaded contractions of single frog cardiac cells. Biophys J Sep 1985;48(3):461–5.
[32] O'Rourke B, Reibel DK, Thomas AP. High-speed digital imaging of cytosolic Ca^{2+} and contraction in single cardiomyocytes. Am J Physiol Jul 1990;259(1 Pt 2):H230–42.
[33] Pollack PS, Carson NL, Nuss HB, Marino TA, Houser SR. Mechanical properties of adult feline ventricular myocytes in culture. Am J Physiol Jan 1991;260(1 Pt 2):H234–41.
[34] Mukherjee R, Crawford FA, Hewett KW, Spinale FG. Cell and sarcomere contractile performance from the same cardiocyte using video microscopy. J Appl Physiol Apr 1993;74(4):2023–33.
[35] Stummann TC, Wronski M, Sobanski T, Kumpfmueller B, Hareng L, Bremer S, et al. Digital movie analysis for quantification of beating frequencies, chronotropic effects, and beating areas in cardiomyocyte cultures. Assay Drug Dev Technol Jun 2008;6(3):375–85.
[36] Kamgoue A, Ohayon J, Usson Y, Riou L, Tracqui P. Quantification of cardiomyocyte contraction based on image correlation analysis. Cytometry A Apr 2009;75(4):298–308.
[37] Bazan C, Barba DT, Blomgren P, Paolini P. Image processing techniques for assessing contractility in isolated adult cardiac myocytes. Int J Biomed imaging 2009;2009:352954.
[38] Bazan C, Torres Barba D, Blomgren P, Paolini P. Image processing techniques for assessing contractility in isolated neonatal cardiac myocytes. Int J Biomed imaging 2011;2011:729732.
[39] Hossain MM, Shimizu E, Saito M, Rao SR, Yamaguchi Y, Tamiya E. Non-invasive characterization of mouse embryonic stem cell derived cardiomyocytes based on the intensity variation in digital beating video. Analyst Jul 2010;135(7):1624–30.
[40] Harmer AR, Abi-Gerges N, Morton MJ, Pullen GF, Valentin JP, Pollard CE. Validation of an in vitro contractility assay using canine ventricular myocytes. Toxicol Appl Pharmacol Apr 15 2012;260(2):162–72.
[41] Harding SE, Vescovo G, Kirby M, Jones SM, Gurden J, Poole-Wilson PA. Contractile responses of isolated adult rat and rabbit cardiac myocytes to isoproterenol and calcium. J Mol Cell Cardiol Jul 1988;20(7):635–47.
[42] Vescovo G, Harding SE, Jones SM, Dalla Libera L, Pessina AC, Poole-Wilson PA. Comparison between isomyosin pattern and contractility of right ventricular myocytes isolated from rats with right cardiac hypertrophy. Basic Res Cardiol Sep–Oct 1989;84(5):536–43.
[43] Steadman BW, Moore KB, Spitzer KW, Bridge JH. A video system for measuring motion in contracting heart cells. IEEE Trans Biomed Eng Apr 1988;35(4):264–72.
[44] He JQ, Ma Y, Lee Y, Thomson JA, Kamp TJ. Human embryonic stem cells develop into multiple types of cardiac myocytes: action potential characterization. Circ Res Jul 11 2003;93(1):32–9.
[45] Brito-Martins M, Harding SE. Ali NN. beta(1)- and beta(2)-adrenoceptor responses in cardiomyocytes derived from human embryonic stem cells: comparison with failing and non-failing adult human heart. Br J Pharmacol Feb 2008;153(4):751–9.
[46] Ahola A, Kiviaho AL, Larsson K, Honkanen M, Aalto-Setala K, Hyttinen J. Video image-based analysis of single human induced pluripotent stem cell derived cardiomyocyte beating dynamics using digital image correlation. Biomed Eng Online 2014;13(1):39.
[47] Hayakawa T, Kunihiro T, Dowaki S, Uno H, Matsui E, Uchida M, et al. Noninvasive evaluation of contractile behavior of cardiomyocyte monolayers based on motion vector analysis. Tissue Eng Part C Methods Jan 2012;18(1):21–32.
[48] Ma J, Guo L, Fiene SJ, Anson BD, Thomson JA, Kamp TJ, et al. High purity human-induced pluripotent stem cell-derived cardiomyocytes: electrophysiological properties of action potentials and ionic currents. Am J Physiol Nov 2011;301(5):H2006–17.
[49] Ghanbari M. The cross-search algorithm for motion estimation. Trans Commun 1990;38(7):950–3.
[50] Dembo M, Wang YL. Stresses at the cell-to-substrate interface during locomotion of fibroblasts. Biophys J Apr 1999;76(4):2307–16.
[51] Sabass B, Gardel ML, Waterman CM, Schwarz US. High resolution traction force microscopy based on experimental and computational advances. Biophys J Jan 1 2008;94(1):207–20.
[52] Tseng Q, Duchemin-Pelletier E, Deshiere A, Balland M, Guillou H, Filhol O, et al. Spatial organization of the extracellular matrix regulates cell–cell junction positioning. Proc Natl Acad Sci U S A Jan 31 2012;109(5):1506–11.
[53] Butler JP, Tolic-Norrelykke IM, Fabry B, Fredberg JJ. Traction fields, moments, and strain energy that cells exert on their surroundings. Am J Physiol Cell Physiol Mar 2002;282(3):C595–605.
[54] Yamazaki K, Hihara T, Taniguchi T, Kohmura N, Yoshinaga T, Ito M, et al. A novel method of selecting human embryonic stem cell-derived cardiomyocyte clusters for assessment of potential to influence QT interval. Toxicol In Vitro Mar 2012;26(2):335–42.
[55] Halbach M, Egert U, Hescheler J, Banach K. Estimation of action potential changes from field potential recordings in multicellular mouse cardiac myocyte cultures. Cell Physiol Biochem 2003;13(5):271–84.
[56] Meyer T, Boven KH, Gunther E, Fejtl M. Micro-electrode arrays in cardiac safety pharmacology: a novel tool to study QT interval prolongation. Drug Saf 2004;27(11):763–72.
[57] Egert U, Meyer T. Heart on a chip — extracellular multielectrode recordings from cardiomyocytes in vitro; 2005.
[58] Reppel M, Igelmund P, Egert U, Juchelka F, Hescheler J, Drobinskaya I. Effect of cardioactive drugs on action potential generation and propagation in embryonic stem cell-derived cardiomyocytes. Cell Physiol Biochem 2007;19(5–6):213–24.
[59] Liang H, Matzkies M, Schunkert H, Tang M, Bonnemeier H, Hescheler J, et al. Human and murine embryonic stem cell-derived cardiomyocytes serve together as a valuable model for drug safety screening. Cell Physiol Biochem 2010;25(4–5):459–66.
[60] Matsa E, Rajamohan D, Dick E, Young L, Mellor I, Staniforth A, et al. Drug evaluation in cardiomyocytes derived from human induced pluripotent stem cells carrying a long QT syndrome type 2 mutation. Eur Heart J Apr 2011;32(8):952–62.
[61] Braam SR, Tertoolen L, van de Stolpe A, Meyer T, Passier R, Mummery CL. Prediction of drug-induced cardiotoxicity using human embryonic stem cell-derived cardiomyocytes. Stem Cell Res Mar 2009;4(2):107–16.
[62] Nomura F, Kaneko T, Hattori A, Yasuda K. On-chip constructive cell-network study (II): on-chip quasi-in vivo cardiac toxicity assay for ventricular tachycardia/fibrillation measurement using ring-shaped closed circuit microelectrode with lined-up cardiomyocyte cell network. J Nanobiotechnol 2011;9:39.
[63] Periasamy M, Bhupathy P, Babu GJ. Regulation of sarcoplasmic reticulum Ca^{2+} ATPase pump expression and its relevance to cardiac muscle physiology and pathology. Cardiovasc Res Jan 15 2008;77(2):265–73.
[64] Borlaug BA, Kass DA. Mechanisms of diastolic dysfunction in heart failure. Trends Cardiovasc Med Nov 2006;16(8):273–9.
[65] Uesugi M, Ojima A, Taniguchi T, Miyamoto N, Sawada K. Low-density plating is sufficient to induce cardiac hypertrophy and electrical remodeling in highly purified human iPS cell-derived cardiomyocytes. J Pharmacol Toxicol Methods 2014;69(2):177–88.
[66] Shinozawa T, Imahashi K, Sawada H, Furukawa H, Takami K. Determination of appropriate stage of human-induced pluripotent stem cell-derived cardiomyocytes for drug screening and pharmacological evaluation in vitro. J Biomol Screen Oct 2012;17(9):1192–203.
[67] Bird SD, Doevendans PA, van Rooijen MA, Brutel de la Riviere A, Hassink RJ, Passier R, et al. The human adult cardiomyocyte phenotype. Cardiovasc Res May 1 2003;58(2):423–34.
[68] Bhana B, Iyer RK, Chen WL, Zhao R, Sider KL, Likhitpanichkul M, et al. Influence of substrate stiffness on the phenotype of heart cells. Biotechnol Bioeng Apr 15 2010;105(6):1148–60.
[69] Hersch N, Wolters B, Dreissen G, Springer R, Kirchgessner N, Merkel R, et al. The constant beat: cardiomyocytes adapt their forces by equal contraction upon environmental stiffening. Biol Open Mar 15 2013;2(3):351–61.
[70] Wang JH, Lin JS. Cell traction force and measurement methods. Biomech Model Mechanobiol Nov 2007;6(6):361–71.
[71] Langer GA, Brady AJ, Tan ST, Serena D. Correlation of the glycoside response, the force staircase, and the action potential configuration in the neonatal rat heart. Circ Res Jun 1975;36(6):744–52.
[72] Zhang J, Wilson GF, Soerens AG, Koonce CH, Yu J, Palecek SP, et al. Functional cardiomyocytes derived from human induced pluripotent stem cells. Circ Res Feb 27 2009;104(4):e30–41.
[73] Honda M, Kiyokawa J, Tabo M, Inoue T. Electrophysiological characterization of cardiomyocytes derived from human induced pluripotent stem cells. J Pharmacol Sci 2011;117(3):149–59.
[74] van der Linde HJ, Van Deuren B, Somers Y, Loenders B, Towart R, Gallacher DJ. The electro-mechanical window: a risk marker for Torsade de Pointes in a canine model of drug induced arrhythmias. Br J Pharmacol Dec 2010;161(7):1444–54.
[75] Guns PJ, Johnson DM, Van Op den Bosch J, Weltens E, Lissens J. The electromechanical window in anaesthetized guinea pigs: a new marker in screening for Torsade de Pointes risk. Br J Pharmacol May 2012;166(2):689–701.
[76] Guns PJ, Johnson DM, Weltens E, Lissens J. Negative electro-mechanical windows are required for drug-induced Torsades de Pointes in the anesthetized guinea pig. J Pharmacol Toxicol Methods Sep 2012;66(2):125–34.
[77] Doss MX, Di Diego JM, Goodrow RJ, Wu Y, Cordeiro JM, Nesterenko VV, et al. Maximum diastolic potential of human induced pluripotent stem cell-derived cardiomyocytes depends critically on I(Kr). PLoS One 2012;7(7):e40288.
[78] Wellens HJ, Tan SL, Bar FW, Duren DR, Lie KI, Dohmen HM. Effect of verapamil studied by programmed electrical stimulation of the heart in patients with paroxysmal re-entrant supraventricular tachycardia. Br Heart J Oct 1977;39(10):1058–66.
[79] Gay R, Algeo S, Lee R, Olajos M, Morkin E, Goldman S. Treatment of verapamil toxicity in intact dogs. J Clin Invest Jun 1986;77(6):1805–11.
[80] Nazzaro P, Manzari M, Merlo M, Triggiani R, Scarano AM, Lasciarrea A, et al. Antihypertensive treatment with verapamil and amlodipine. Their effect on the functional autonomic and cardiovascular stress responses. Eur Heart J Sep 1995;16(9):1277–84.